Emission Control Science and Technology
https://doi.org/10.1007/s40825-019-00139-w

SPECIAL ISSUE: 2018 CLEERS WORKSHOP, SEPTEMBER 18-20, ANN ARBOR, MICHIGAN, UNITED STATES

Palladium/Zeolite Low Temperature Passive NOx Adsorbers (PNA): Structure-Adsorption Property Relationships for Hydrothermally Aged PNA Materials

Konstantin Khivantsev[1] · Nicholas R. Jaegers[1] · Libor Kovarik[1] · Jian Zhi Hu[1] · Feng Gao[1] · Yong Wang[1] · János Szanyi[1]

Received: 7 February 2019 / Revised: 20 August 2019 / Accepted: 23 August 2019

Abstract

Zeolites with different framework structures (SSZ-13, ZSM-5, BEA) but similar Si/Al ratios (~ 12–15) and Pd loading (~ 1 wt%) were synthesized and evaluated as low-temperature passive NOx adsorbers (PNA). These materials exhibit high NOx adsorption efficiency with atomically dispersed Pd being the active adsorption site. Hydrothermal aging at 750 °C for 16 h in the presence of 10% water vapor in air resulted in the formation of PdO nanoparticles in all three samples as evidenced by high-energy XRD. Hydrothermal aging of the small-pore 1–3 wt% Pd/SSZ-13 (Si/Al = 6) materials, which contain ~ 100–90% atomically dispersed palladium ions, decreases its PNA performance only by ~ 10–20%, indicating agglomeration of only ~ 10–20% of atomically dispersed Pd into PdO. High-field solid state ^{27}Al NMR studies on the fresh and aged samples reveal dealumination and significant changes in the distribution of Al (and thus, Brönsted acid) sites after hydrothermal aging. FTIR measurements with NO probe molecule and titration of Brönsted acid sites with nitrosyl (NO^+) ions further corroborate the ^{27}Al NMR data. Because framework aluminum atoms are the anchoring sites for atomically dispersed Pd ions, their elution from the framework causes the loss of active atomically dispersed Pd species. With the aid of HAADF-STEM imaging and synchrotron XRD studies, we further confirm and visualize the fate of these Pd species: they agglomerate into PdO nanoparticles on the external surface of zeolite. Consequently, these changes lead to the decrease in PNA performance of these materials after hydrothermal aging. The thus formed PdO agglomerates cannot be re-dispersed back to their ionic state due to the loss of framework Al T-sites and/or inherent stability of such large PdO particles. Our study demonstrates that, unlike in previous studies that found increased PNA performance upon HTA, high temperatures hydrothermal aging of PNA materials that contain atomically dispersed Pd initially results in a decrease in NOx storage efficiency due to the formation of PdO agglomerates. However, we also highlight the high hydrothermal stability of predominantly atomically dispersed 1–3 wt% Pd/SSZ-13 (Si/Al = 6), whose performance decreases only marginally after prolonged hydrothermal aging at 750 °C. This study shows that hydrothermally stable passive NOx materials can be prepared using small-pore SSZ-13 zeolite.

Keywords Palladium · Zeolite · Passive NOx adsorber (PNA) · High-field magic angle spinning 27Al NMR · HAADF-STEM imaging · FTIR · Hydrothermal aging

1 Introduction

In order to improve the health of the population and decrease the rate of climate change, abatement of toxic and environmentally harsh nitric oxides from the vehicle exhaust is critical [1]. The selective catalytic reduction (SCR) technology achieves this. More specifically, cooper/zeolite (SSZ-13) catalysts and the injected urea/ammonia source are employed [2, 3]. These catalytic materials are very active at temperatures > 180–200 °C. However, during cold start and idle operations

Konstantin Khivantsev, Nicholas R. Jaegers and Libor Kovarik contributed equally to this work.

✉ János Szanyi
Janos.Szanyi@pnnl.gov

[1] Institute for Integrated Catalysis, Pacific Northwest National Laboratory, Richland, WA 99352, USA

Published online: 04 September 2019

(temperatures below 150 °C), Cu/zeolite materials are not effective for the transformation of NOx to N_2 [2, 3]. In order to circumvent the low-temperature NOx abatement issue, passive NOx adsorbers (PNA) materials have recently been disclosed [4–13]. These materials store NOx at low temperatures (~ 100 °C) and release them continuously at higher temperatures > 200 °C when Cu/zeolite SCR catalysts become active. This array of materials includes platinum dispersed on alumina and various doped/modified alumina [6, 9], Pd and Pt on ceria-containing materials [10]. Unfortunately, such oxide-based materials store only relatively low amounts of NOx and are susceptible to sulfur poisoning and are hydrothermally unstable. The Jonson Matthey team, first, and then others, reported Pd/zeolite formulations [7–19] on SSZ-13, BEA, and ZSM-5 zeolites, with considerable NOx storage at 100 °C and release above 200 °C. The chemistry of Pd/Zeolite formulations remained poorly understood until recently, when various storage avenues for NOx on Pd/SSZ-13 and Pd/BEA model materials were proposed [15, 18, 19]. For the first time, we showed that in the presence of just NO, Pd(I) and Pd(II) NO complexes are formed. When both NO and O_2 are present, palladium nitrosyl complexes and nitrosonium (alternatively called "nitrosyl") NO^+ ions in ion-exchange positions contribute to storage, while under practical conditions (NO, CO, H_2O, O_2, N_2), the PNA performance of materials is largely due to formation of a stable mixed carbonyl/nitrosyl palladium complex, Pd(II)(NO)(CO) both on Pd/SSZ-13 and Pd-BEA. Also, we revealed the important dependence of PNA performance of Pd/BEA on the zeolite crystal size with similar Si/Al ratios. The common factor for all those materials is that atomically dispersed Pd species in zeolite micropores are the active sites for PNA adsorption, while larger PdO nanoparticles are inactive. We also recently showed that unprecedented super electrophilic M(II) (e.g., Pd) species are stabilized very selectively in SSZ-13 and responsible for the unique spectroscopic and performance features of those materials [20].

Despite significant advances in our molecular level understanding of PNA performance of Pd/zeolite materials, the changes in their structure/properties upon hydrothermal aging are not fully understood and therefore need to be studied. Some reports suggested that the PNA performance could be improved upon hydrothermal aging. As we have recently pointed out, in those reports, the initial state of Pd was a mixture of Pd in ion exchange sites (atomically dispersed Pd) and PdO nanoparticles. The latter represent the majority of species, rendering a significant fraction of expensive Pd in those samples inactive from the start. If we start with well-dispersed materials with high Pd dispersion (such materials represent the most effective passive NOx adsorbers known [18, 19]), the effects of hydrothermal aging are of utmost importance to elucidate because in the vehicle, these materials are subject to high-temperature treatments with high water content during high-load operation and diesel particulate filter (DPF) regeneration. In order to understand the HTA effects, we use the synchrotron XRD technique to compare Pd/Zeolite materials (ZSM-5, BEA, and SSZ-13) before and after hydrothermal aging. This technique exhibits much higher sensitivity to small amounts of crystalline phases than regular XRD. Moreover, for the Pd/SSZ-13 samples, we performed PNA evaluation before and after hydrothermal aging. This, combined with FTIR data with NO as a probe molecule, as well as HAADF-STEM imaging of samples before and after hydrothermal aging, coupled with solid state ^{27}Al NMR studies, allowed us to fully clarify the mechanism of deactivation of such materials as a result of hydrothermal aging. The obtained structure-adsorption property relationships allow us to highlight the superior performance of Pd/SSZ-13 passive NOx adsorber materials, which lost only 10–15% of its adsorption capacity after HTA at 750 °C for 16 h.

2 Experimental Methods

NH_4-BEA crystals with Si/Al ~ 12.5–13 was supplied by Zeolyst. To transform it into H-form, it was calcined at 550 °C in static air.

NH_4-ZSM-5 with Si/Al_2 ratio 25 was supplied by Zeolyst. To transform it into H-form, it was calcined at 550 °C in static air.

H-ZSM-5 with Si/Al ratio ~ 300 (this sample is called "MFI" in the manuscript, as this particular term for highly siliceous ZSM-5 material is widely used) was supplied by Tricat and used after 550 °C calcination in static air.

Na/SSZ-13 zeolite with Si/Al 6 and 12 was hydrothermally synthesized using the following recipe, 0.8 g of NaOH (Sigma-Aldrich, ≥ 99%) was dissolved in 50 ml of deionized water. Then, 17 g of TMAda-OH (Sachem Inc., 25% N,N,N-trimethyl-1-adamantyl ammonium hydroxide) was added as structure directing agent. Consequently, 1.5 g of $Al(OH)_3$ (Sigma-Aldrich, ~ 54% Al_2O_3) was slowly added to the solution and stirred at 400 rpm until it was completely dissolved. Afterwards, 20.0 g of LUDOX HS-30 colloidal silica (Sigma-Aldrich, 30 wt% suspension in H_2O) was added slowly to the solution until a uniform white gel was formed. The obtained gel was sealed in a 125-mL Teflon-lined stainless steel autoclave containing a magnetic stir bar. Hydrothermal synthesis was carried out at 160 °C under continuous gel stirring at 400 rpm for 4 days. After synthesis, the zeolite cake was separated from the suspension by centrifugation, and washed three times with deionized water. It was then dried at 80 °C under N_2 flow overnight, and calcined in air at 550 °C for 5 h in order to remove the SDA. NH4/SSZ-13 was obtained by ion exchange of the as-prepared Na/SSZ-13 zeolite with 0.5 M NH4NO3 solution at 80 °C for 5 h. The process was repeated three times.

For H-forms of zeolite, the regular incipient wetness impregnation method was used to obtain 1 wt% Pd/Zeolite powders. They were subsequently dried at 80 °C and subsequently calcined at 600 °C in static air.

Samples with ~ 100 and 90% of atomically dispersed Pd for 1 and 3 wt% Pd loadings on SSZ-13 were prepared by modified ion exchange (for Pd) with 10 wt% $Pd(NH_3)_4(NO_3)_2$ solution (Sigma-Aldrich 99.99%) with NH_4-SSZ-13 with Si/Al ratio 6. More specifically, a minimum amount of the Pd(II) precursor solution was added to zeolite in the amount approximately equivalent to the total pore volume of the zeolite. The thick paste was mixed and stirred vigorously for 30 min, followed by calcination in air at 600 °C for 5 h (ramping rate 2 °C/min).

Hydrothermal aging (HTA) was performed at 750 °C for 16 h in a flow reactor with GHSV ~ 340 K. The gas mix, used for HTA, contains air and 10% H_2O.

The in situ static transmission FTIR experiments were conducted in a home-built cell housed in the sample compartment of a Bruker Vertex 80 spectrometer, equipped with an MCT detector and operated at 4 cm^{-1} resolution. The powder sample was pressed onto a tungsten mesh which, in turn, was mounted onto a copper heating assembly attached to a ceramic feedthrough. The sample could be resistively heated, and the sample temperature was monitored by a thermocouple spot welded onto the top center of the W grid. The cold finger on the glass bulb containing CO was cooled with liquid nitrogen to eliminate any contamination originating from metal carbonyls, while NO was cleaned with multiple freeze–pump–thaw cycles. Prior to spectrum collection, a background with the activated (annealed, reduced, or oxidized) sample in the IR beam was collected. Each spectrum reported is obtained by averaging 256 scans. The spectra were recorded via sequential adsorption of precisely measured aliquots of NO.

HAADF-STEM analysis was performed with a FEI Titan 80-300 microscope operated at 300 kV. The instrument is equipped with a CEOS GmbH double-hexapole aberration corrector for the probe-forming lens, which allows for imaging with 0.1 nm resolution in scanning transmission electron microscopy mode (STEM). The images were acquired with a high-angle annular dark field (HAADF) detector with inner collection angle set to 52 mrad.

^{27}Al MAS NMR measurements were performed at room temperature on a Bruker 850 MHz NMR spectrometer, operating at a magnetic field of 19.975 T. The corresponding ^{27}Al Larmor frequency is 221.412598 MHz. All spectra were acquired at a sample spinning rate of 18.7 kHz (± 5 Hz) and externally referenced to 1.0 M aqueous $Al(NO_3)_3$ (0 ppm). The advantages of both enhanced spectral resolution and sensitivity for acquiring ^{27}Al MAS NMR at ultrahigh field (19.975 T) have been established previously.

Cryo High-energy X-ray Diffraction (XRD) data were collected at beamline 11-ID-B at the Advanced Photon Source at Argonne National Laboratory using 58.6 keV (0.2114 Å) X-rays. Samples were loaded in the powder form in low-background Kapton capillary holders, and cooled using liquid nitrogen microjets. Data were collected using amorphous silicon-based area detectors. Geometric corrections and reduction to one-dimensional data used GSAS-II. PDFs were obtained from the data using pdfgetX315 to a Q max = 24 $Å^{-1}$.

Standard NOx adsorption tests were conducted in a plug-flow reactor system with powder samples (120 mg, 60–80 mesh) loaded in a quartz tube, using a synthetic gas mixture that contained 200 ppm of NOx or (200 ppm of NOx and 14% O_2) balanced with N_2 at a flow rate of 210 and 310 sccm (corresponding to 220,000 and 340,000 h^{-1} in which we consider the density of zeolite to be ~ 2.1 g/cc). All the gas lines were heated to over 100 °C. Concentrations of reactants and products were measured by an online MKS MultiGas 2030 FTIR gas analyzer with a gas cell maintained at 191 °C. Even though it is preferable to use a pure NO feed for the study, the actual NOx feed contained ~ 185 ppm of NO and ~ 15 ppm of NO_2, where the latter came from the NO source and background NO oxidation by the heated gas lines. Since realistic engine exhausts do contain ~ 5% of NO_2 in the total NOx, no effort was made to remove NO_2 from our feed. Two-four-way valves were used for gas switching between the reactor and the bypass. Prior to storage testing at 100 °C, the sample was pretreated in 14% O_2 balanced in N_2 flow for 1 h at 550 °C and cooled to the target temperature in the same feed. The gas mixture was then switched from the reactor to the bypass, and 200 ppm of NOx was added to the mixture. Upon stabilization, the gas mixture was switched back from bypass to the reactor for storage testing for 10 min. The sample was then heated to 600 °C at a rate of 10 °C/min to record the desorption profiles of gases in the effluent.

3 Results and Discussion

3.1 NO_x Storage Performance of 1 Wt% Pd/Zeolite Materials: Establishing the Importance of Brönsted Acid Sites

Figure 1 shows NOx trapping followed by temperature-programmed desorption (TPD) of NO_x for 1 wt% Pd/Zeolite materials with Si/Al ~ 12, prepared via regular IWI with H-forms of zeolites for BEA, ZSM-5, and SSZ-13. These samples were the baseline for our investigation of these materials. During the first 10 min of gas phase analysis, the feed ran through the bypass line. At $t = 10$ min, the feed was switched to the reactor. At $t = 20$ min, the temperature ramp up was initiated at a linear rate of 10 °C/min to desorb the trapped NO_x. The measurement was stopped shortly after the sample temperature reached 600 °C. Since the NOx inlet concentration was ~ 200 ppm, in the 10–20-min time-on-stream

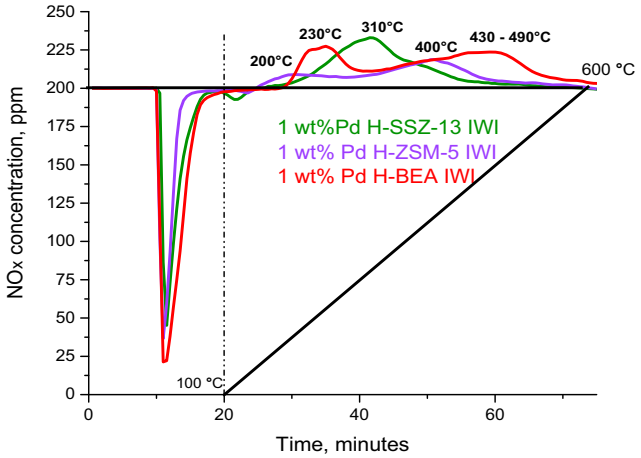

Fig. 1 NOx adsorption at 100 °C for 10 min followed with TPD (10 °C/min linear ramp rate). Conditions, 120 mg of the sample, 210 sccm/min flow rate. The feed gas mixture contains ~200 ppm of NOx (190 ppm of NO and 10 ppm of NO_2) balanced with N_2 at a flow rate of 210 sccm with 14% O_2, 200 ppm CO, and 2.7% H_2O. Note that during the first 10 min of data recording, the feed gas runs through a bypass line

interval, the integrated negative peaks below 200 ppm represented NO_x storage capacity, and beyond 20 min, the positive peaks above 200 ppm corresponded to NO_x released. Clearly, all tested materials are capable of storing NOx at low temperature (100 °C) and releasing it above 200 °C.

The desorption profiles in Fig. 1 indicate that the NOx release temperatures vary significantly with the type of zeolite framework the Pd was loaded onto. For ZSM-5, the two desorption maxima are at 160 and 410 °C. For the BEA material, the maxima are 200 and 480 °C, whereas for the SSZ-13 the maxima are at 300 and (the low intensity peak) 400 °C. A simple qualitative comparison clearly indicates that Pd/SSZ-13 with its NOx release maxima between 300 and 400 °C represents the most attractive material in terms of the release temperature followed by Pd/BEA and then Pd/ZSM-5. The NO/Pd storage ratios summarized in Table 1 also show that the storage capacity for these materials seems to follow the same trend, with 1 wt% Pd/SSZ-13 and 1 wt% Pd/BEA storing more NOx than 1 wt% Pd/ZSM-5.

One question that immediately arises at this point: do we really need to use zeolites that contain Bronsted acid sites (i.e., having Al in the framework)? Although, in the Pd/zeolite PNA literature the studies focus on H-forms of zeolites [8, 11, 13–15, 18–20], we decided to investigate this point by:

Table 1 NOx storage capacity of 1 wt% Pd/Zeolite materials for SSZ-13, BEA, and ZSM-5 zeolite with Si/Al ratio ~ 12 for all model zeolites

Material (Si/Al ~ 12)	NOx/Pd ratio	NOx storage capacity (μmol/g)
1 wt% Pd/SSZ-13	0.43	40
1 wt% Pd/BEA	0.53	50
1 wt% Pd/ZSM-5	0.3	28

(1). Replacing the Bronsted acid sites with Na ions (we performed exchange with the Na form of zeolite instead of H-form). (2) Loading Pd into the sample of silicalite-1 (also called MFI, which is the analogue of ZSM-5 with fewer Al) that has very high Si/Al ratio (> 300) thus lacks Bronsted acid protons.

The measured PNA storage/release curves of such materials with 1 wt% Pd loading are displayed in Fig. 2. It becomes immediately obvious that the absence of Brönsted acid protons (Al) in the framework of silicalite-1 eliminates virtually all NOx storage ability of the sample.

As we have previously demonstrated, indeed Pd ions replaced sites created by the presence of Al atoms in the framework (in the H-form of zeolite, Bronsted acid protons) and that is the key requirement of their high dispersion [18, 19]. Although, often times higher Si/Al ratios favor higher hydrothermal stability, this leads to agglomeration of Pd into inactive PdOx agglomerates, and the PNA storage capacity is lost.

The Na-form of zeolite SSZ-13 with Si/Al = 6 was also used to support 1 wt% Pd. The individual gas profiles during NOx storage/release of this material (Fig. 3) show complicated behavior. Multiple NOx uptake peaks appear, and the drop of NOx concentration under isothermal storage conditions at 100 °C is much lower than that on the H-form-exchanged sample (the dip ~ 110 ppm vs. ~ 200 ppm initially).

Therefore, using Na (and other monovalent ion)-forms of zeolites to support Pd via ion-exchange of Pd with the Na-form of zeolite is detrimental for PNA activity. These results emphasize the importance of the presence of abundant Brönsted acid protons in the active PNA materials. Such

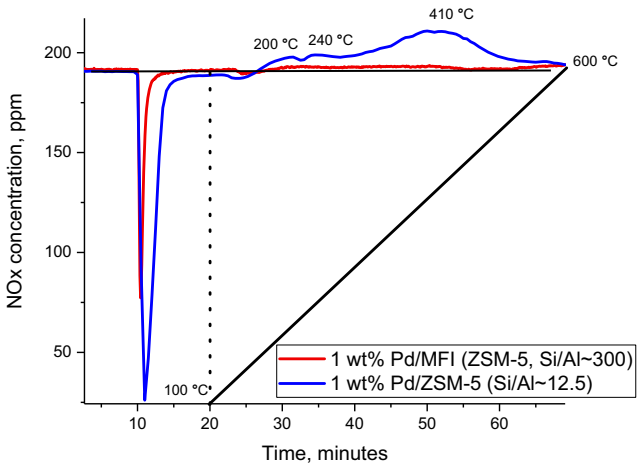

Fig. 2 NOx adsorption at 100 °C for 10 min followed with TPD (10 °C/min linear ramp rate) for 1 wt% Pd/ZSM-5 Si/Al = 12 (blue curve) and 1 wt% Pd/ZSM-5 Si/Al = 300 (red curve). Conditions, 120 mg of the sample, 210 sccm/min flow rate. The feed gas mixture contains ~200 ppm of NOx (190 ppm of NO and 10 ppm of NO_2) balanced with N_2 at a flow rate of 210 sccm with 14% O_2, 200 ppm CO, and 2.7% H_2O. During the first 10 min of data recording, the feed gas runs through a bypass line

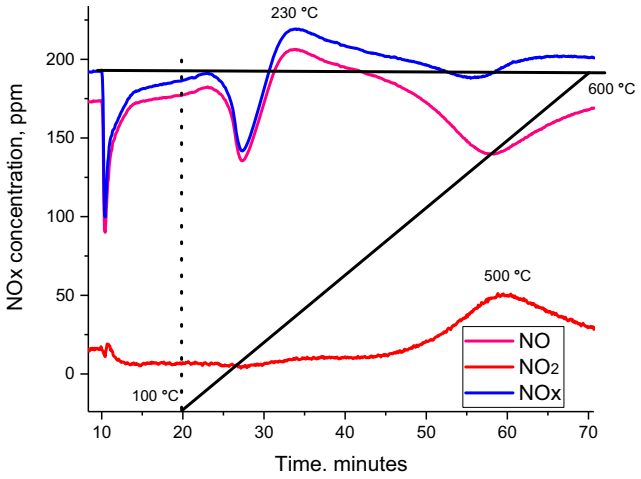

Fig. 3 Individual gas profiles during PNA for 1 wt% Pd/Na-SSZ-13 Si/Al = 6. NOx adsorption at 100 °C for 10 min followed with TPD (10 °C/min linear ramp rate) for. Conditions, 120 mg of the sample, 210 sccm/min flow rate. The feed gas mixture contains ~200 ppm of NOx (190 ppm of NO and 10 ppm of NO_2) balanced with N_2 at a flow rate of 210 sccm with 14% O_2, 200 ppm CO, and 2.7% H_2O. During the first 10 min of data recording, the feed gas runs through a bypass line

protons are either formed after NH_4-Zeolite thermal decomposition to H-Zeolite, or they are initially present as H-sites.

3.2 XRD Studies of Fresh and Hydrothermally Aged Pd/Zeolite Model Materials

Since hydrothermal stability of NOx abatement materials is a crucial factor that affects their long-term performance in vehicles, we explored the changes of these baseline materials after hydrothermal aging (750 °C, 16 h, 10% water vapor in air flow) using synchrotron XRD. We applied synchrotron XRD because it is much more sensitive than conventional XRD that normally fails to detect < 0.5 wt% of nanoparticles on solid supports (Figs. 4, 5 and 6).

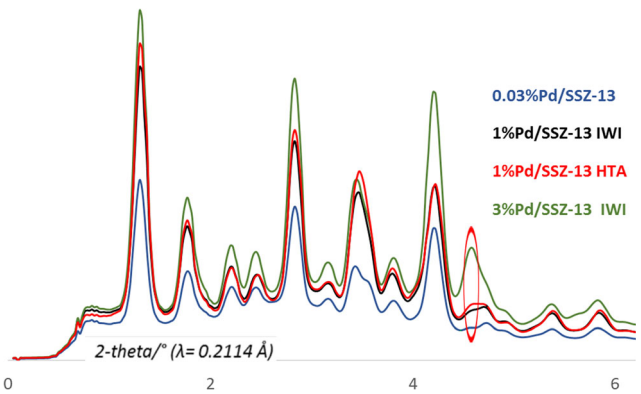

Fig. 4 High-energy XRD profile for Pd/SSZ-13 Si/Al ~ 12 fresh and aged samples with different loadings of Pd (HTA denotes hydrothermally aged sample, IWI denotes incipient wetness impregnation)

Note that the wavelength of the X-ray in these measurements is 0.2114 Å, therefore the spectra are "compressed" along the 2Theta axis compared to traditional (copper radiation, lambda ~ 1.5406 Angstroms) XRD.

Figure 4 indicates that upon hydrothermal aging, a new diffraction peak appears at 4.7° in the XRD pattern. Compared to conventional XRD, this corresponds to 34°, where PdO signature in XRD usually appears [21]. Therefore, we can conclude that upon HTA PdO nanoparticles appear in the 1 wt% Pd/SSZ-13 sample. A similar conclusion can be drawn for the 1 wt% Pd/ZSM-5 material: upon aging, the formation of PdO is observed. The low intensity of the observed PdO peak suggests that only small amounts of PdO are formed. However, for the 1 wt% Pd/BEA material, the formation of PdO is not obvious upon HTA.

Comparison of the pair distribution function (PDF) data for the fresh and aged 1 wt% Pd/SSZ-13 (Fig. 7) indicates the presence of an additional phase in the aged sample with distances 2.01, 3.07, and 3.43 Å. These values agree well with 4 Pd-O, 4 Pd-Pd, and 8 Pd-Pd bond distances observed for well-defined PdO nanoparticles. This further suggests that predominantly large PdO nanoparticles form upon aging, and not metallic Pd or small PdO clusters. In conclusion, HTA of 1 wt% Pd/SSZ-13 material leads to the formation of PdO nanoparticles, most probably on the external surface of the zeolite, owing to the fact that the micropores of SSZ-13 are unable to confine species larger than ~ 0.85 nm which is the maximum cage diameter in SSZ-13.

3.3 Investigation of PNA Performance of Aged 1–3 Wt% Pd/SSZ-13 Samples with Varying Si/Al Ratios

In order to get further insight into the effect of hydrothermal aging on the NOx storage/release (PNA) properties of aged materials, we performed studies under practically relevant conditions on the fresh and aged samples of 1–3 wt% Pd/SSZ-13 with Si/Al ~6, 12, and 30 as well as 1 wt% Pd/BEA with Si/Al ~ 12. The samples were prepared according to [18], in order to maximize Pd dispersion.

For the investigation of the effect of the Si/Al ration on the on hydrothermal aging, we choose three SSZ-13 zeolites with Si/Al ratios 6, 12, and 30, and identical (1 wt%) Pd loading. As we have reported previously, the respective NOx/Pd ratios are ~ 1, 0.9, and 0.3, indicating that approximately 100, 90, and 30% of Pd is atomically dispersed in these samples. The corresponding HAADF-STEM images of the samples [18] show progressive agglomeration of PdO in the fresh samples with the increase in Si/Al ratio: fully atomic dispersion for the sample with Si/Al ratio 6, mostly atomic dispersion with 1–2 nm PdO clusters for the sample with Si/Al = 12, and PdO nanoparticles larger > 10 nm on the external surface of the

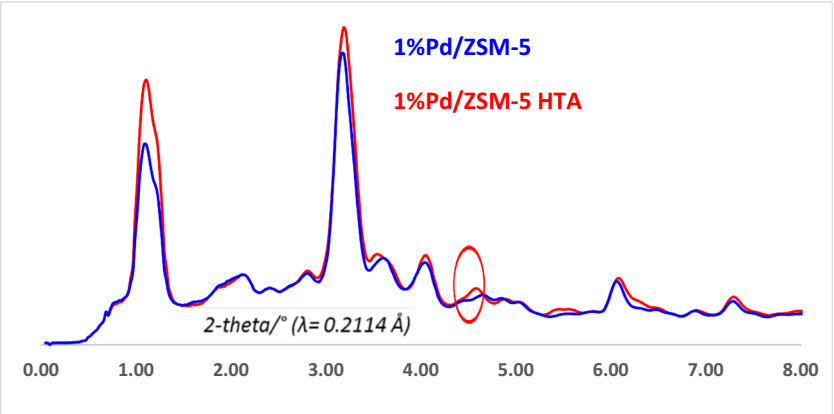

Fig. 5 High-energy XRD profile for fresh and aged Pd/ZSM-5 samples with Si/Al ~ 12, prepared via IWI (incipient wetness impregnation)

sample with Si/Al ~ 30. With increasing Si/Al ratio, the micropores of the SSZ-13 zeolite become less hydrophilic which leads to its inability to fully disperse Pd, consequently leading to agglomeration. This important finding [18] suggests that zeolites with high Si/Al ratios (> 10) are not ideal for the preparation of Pd-based PNAs. After hydrothermal aging (16 h at 750 °C), the NOx storage capacity of all three materials studied (Figs. 8, 9 and 10) decreased to a different extent. The loss of performance (NOx uptake) is about 10% for the sample that initially contained mostly atomically dispersed Pd (Si/Al ~ 6), about 50% for the 1 wt% Pd/SSZ-13 with Si/Al = 12, and 10% for the 1 wt% Pd/SSZ-13 with Si/Al = 30 (note, however, that the hydrothermally aged 1 wt% Pd/SSZ-13 with Si/Al ~ 12 still performs better than the fresh 1 wt% Pd/SSZ-13 with Si/Al ~ 30). An important common feature of the desorption curves is the decrease of the intensity of the second desorption feature after HTA (~ 400 °C). In contrast, the lower-temperature desorption feature (at ~ 300 °C) marginally increased for samples with Si/Al ratio 6 and 30, while it decreased for the sample with Si/Al ratio 12. Similar decrease in performance (~ 45%) occurs for the 1 wt% Pd/BEA sample with Si/Al ~ 12 (Fig. 11). It is important to note that 1-3 wt% Pd/SSZ-13 samples with Si/Al ratio 6 have the majority of Pd(II) ions held near pairs of aluminium framework atoms as we spectroscopically proved in our previous work [18, 20]. However, as the Si/Al ratio increases, the numer of paired Al sites to stabilize isolated Pd(II) ions decreases, and Pd may be additionally present as Pd(II)-OH moieties held near 1 Al framework atom. Our results suggest that Pd(II) isolated ions may have higher hydrothermal stability than Pd(II)-OH sites.

Thus, the steam is able to "tear" atomically dispersed Pd from the framework via hydrolysis at elevated temperatures: $Pd(II)/2\ Zeo\text{-}O^{-} + 2\ H_2O \rightarrow Pd(OH)_2 + 2\ Zeo\text{-}OH$.

3.4 Insight into the Structural Changes of Fresh and HTA Pd/SSZ-13 Materials with Varying Si/Al Ratios from Solid-State MAS 27Al NMR

In order to understand the changes at the molecular level, we turned to the magic angle spinning solid-state NMR technique which is known to provide invaluable information on the Al, and thus proton, distribution in zeolites: we performed high-field magic angle spinning (MAS) ^{27}Al NMR experiments on both fresh and aged Pd/SSZ-13 samples [19, 22–26] (Fig. 12).

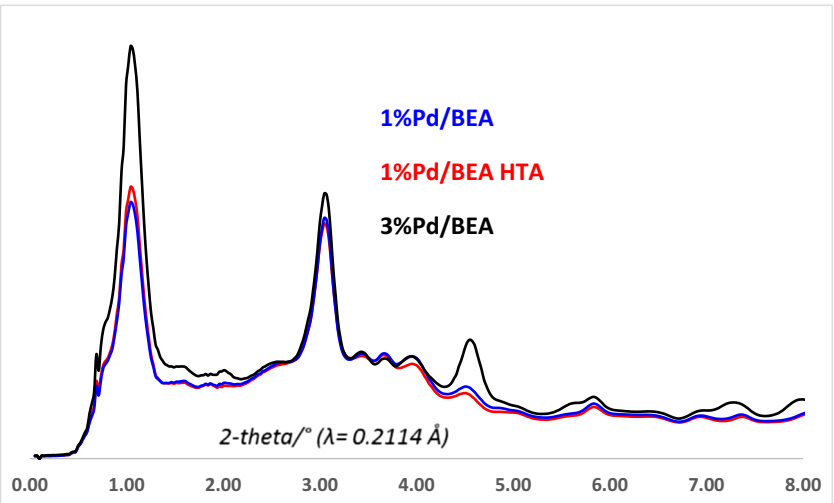

Fig. 6 High-energy XRD profile for fresh and aged 1–3 wt% Pd/BEA samples with Si/Al ~ 12 prepared via IWI (incipient wetness impregnation)

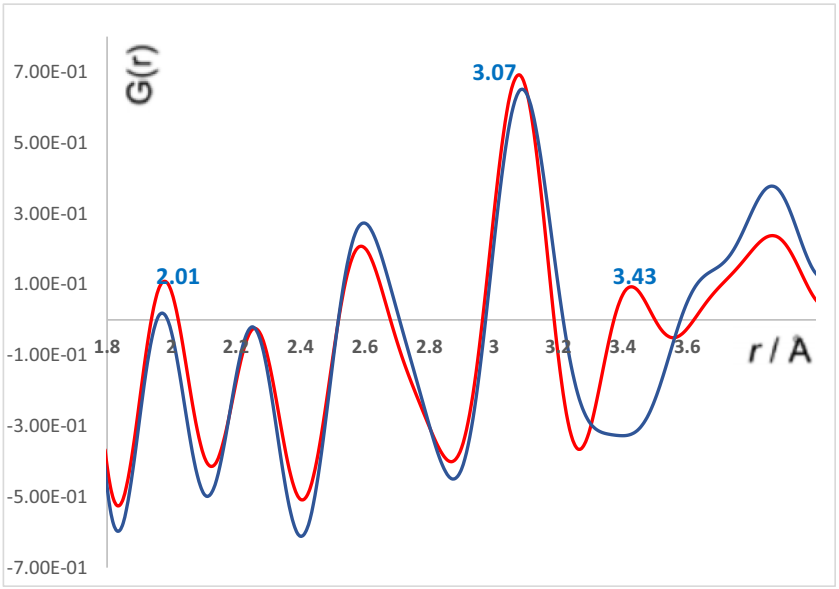

Fig. 7 PDF plots (G(r) vs. r (Angstroms)) for 1 wt% fresh Pd/SSZ-13 (blue line) and aged 1 wt% Pd/SSZ-13 (red line) with Si/Al ~ 12

In fresh Pd/SSZ-13 samples, we observe the presence of a few relatively uniform framework tetrahedral aluminum sites, evidenced by the narrowness of the band (compare, for example, with the broader bands of aged samples), as well as a small fraction of non-framework octahedral Al sites as evidenced by the signal around ~ 0 ppm. After hydrothermal aging, significant changes occur to the Al site distribution. Specifically, substantial decrease and broadening in the intensity of the NMR peak representing tetrahedrally coordinated (i.e., framework) Al atoms: such broadening indicates multiple, less uniform bonding environments present around Al T-sites compared with the fresh samples. This is caused by dealumination, with the concomitant significant increase in the number of extra-framework penta-coordinated Al sites [22–25, 27] as well as some smaller increase in the number of octahedral extra framework Al sites. The decrease in the number and uniformity of framework tetrahedral Al atoms leads to the loss of PNA performance. Simultaneously, increase in the number of penta-coordinated Al sites does not replenish this loss of performance. This can be intuitively understood in a rather simple way. We have already shown that atomically dispersed Pd was the active site for NOx uptake [18–20]. Due to steam-treatment at such high temperatures (750 °C), dealumination inevitably occurs (see NMR data above). The consequences of dealumination are discussed in the following section 3.6.

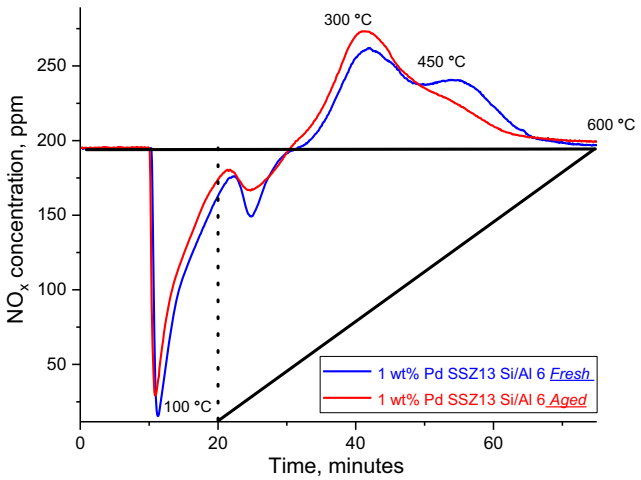

Fig. 8 NOx adsorption at 100 °C for 10 min followed with TPD (10 °C/min linear ramp rate) for 1 wt% Pd/H-SSZ-13 Si/Al = 6 (fresh and aged). Conditions, 120 mg of the sample, 210 sccm/min flow rate. The feed gas mixture contains ~ 200 ppm of NOx (190 ppm of NO and 10 ppm of NO_2) balanced with N_2 at a flow rate of 210 sccm with 14% O_2, 200 ppm CO, and 2.7% H_2O

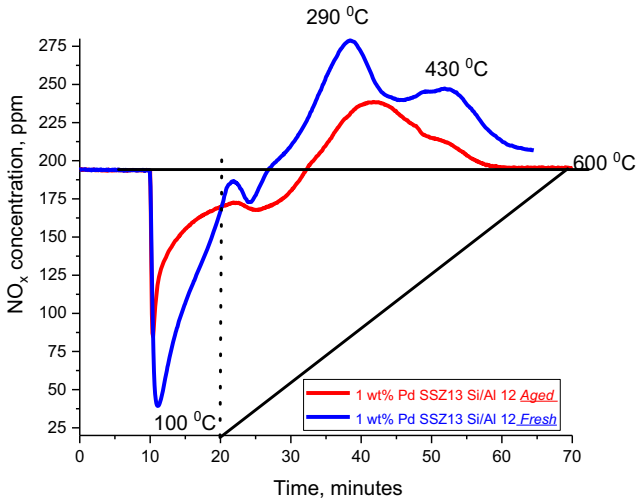

Fig. 9 NOx adsorption at 100 °C for 10 min followed with TPD (10 °C/min linear ramp rate) for 1 wt% Pd/H-SSZ-13 Si/Al = 12. Conditions, 120 mg of the sample, 210 sccm/min flow rate. The feed gas mixture contains ~ 200 ppm of NOx (190 ppm of NO and 10 ppm of NO_2) balanced with N_2 at a flow rate of 210 sccm with 14% O_2, 200 ppm CO, and 2.7% H_2O

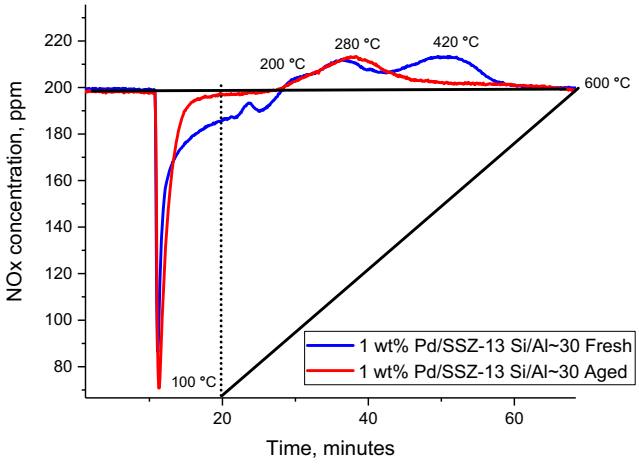

Fig. 10 NOx adsorption at 100 °C for 10 min followed with TPD (10 °C/min linear ramp rate) for 1 wt% Pd/H-SSZ-13 Si/Al = 30. Conditions, 120 mg of the sample, 210 sccm/min flow rate. The feed gas mixture contains ~ 200 ppm of NOx (190 ppm of NO and 10 ppm of NO_2) balanced with N_2 at a flow rate of 210 sccm with 14% O_2, 200 ppm CO, and 2.7% H_2O

3.5 HAADF-STEM Evidence of Bulk-like PdO Formation after Hydrothermal Aging (HTA) of Pd/SSZ-13: Inertness of Large PdO toward Redispersion and the Effects of Reducing Pre-treatment on the PNA Performance of Pd/SSZ-13

Since framework Al ions are the anchoring sites for Pd ions, i.e., Pd atoms replace Bronsted acid protons opposite the Al atom, in the dealuminated samples, the number of these anchoring sites is reduced; therefore, PdO (and/or $Pd(OH)_2$) moieties are free to move around and eventually agglomerate. Indeed, if that was the case, HAADF-STEM images would be

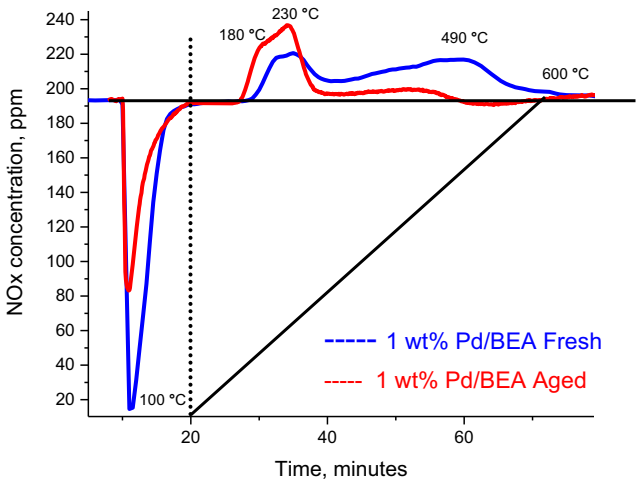

Fig. 11 NOx adsorption for 1 wt% Pd/BEA with Si/Al ~ 12 at 100 °C for 10 min followed with TPD (10 °C/min linear ramp rate). Conditions, 120 mg of the sample, 210 sccm/min flow rate. The feed gas mixture contains ~ 200 ppm of NOx (190 ppm of NO and 10 ppm of NO_2) balanced with N2 at a flow rate of 210 sccm with 14% O2, 200 ppm CO, and 2.7% H_2O

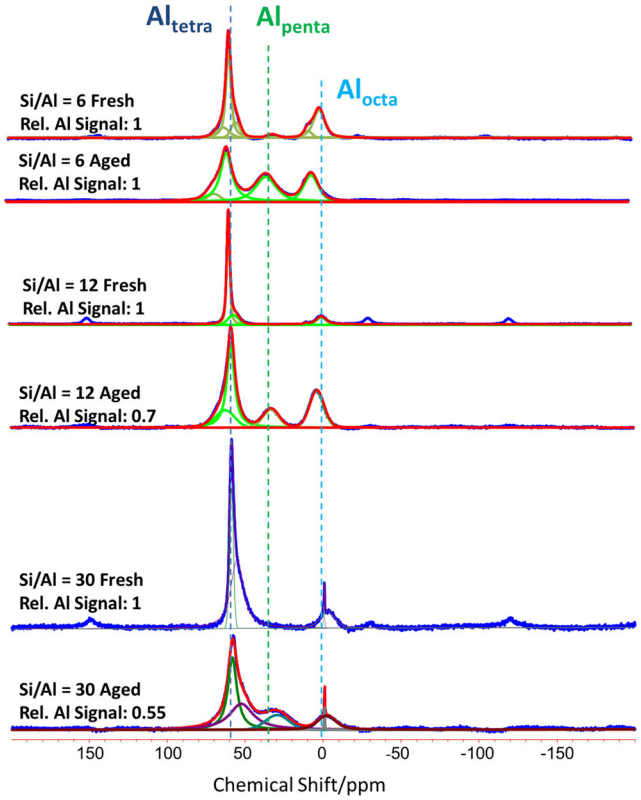

Fig. 12 High-field ^{27}Al MAS-NMR data for the fresh and aged 1 wt% Pd/SSZ-13 samples with varying Si/Al ratios and the corresponding site distribution, denoted as Al octa (for octahedral sites), Al penta (for penta-coordinated sites), and Al tetra (for tetrahedral framework Al sites). All spectra are background-subtracted and relative intensities referenced to the fresh sample of each Si/Al

able to directly show the consequences of dealumination. Since the 1 wt% Pd/SSZ-13 sample with Si/Al ~ 6 has essentially all Pd atomically dispersed (Fig. 13), this was the best sample to look at after HTA (since other samples already have PdO nanoparticles besides atomically dispersed Pd, the effect would not be so obvious).

HAADF-STEM images of the 1 wt% Pd/SSZ-13 Si/Al ~ 6 sample after hydrothermal aging are displayed in Fig. 14.

The formation of > 10–20 nm nanoparticles can clearly be seen for the HTA sample. We are able to resolve the facets of the particles formed, which revealed that they were not metallic Pd, but palladium oxide nanoparticles. This further corroborates the conclusions reached based on the NMR and XRD studies: after loss of framework Al, isolated Pd species become mobile and agglomerate into PdO particles. Apparently, this is the mechanism of deactivation of Pd/Zeolite materials, in particular Pd/SSZ-13. However, we highlight the relatively high stability of atomically dispersed 1–3 wt% Pd/SSZ-13 (prepared on SSZ-13 with Si/Al = 6). The 1 wt% Pd/SSZ-13 sample loses only ~ 10% of its initial activity after 16 h of hydrothermal aging at 750 °C in 10% H_2O vapor. Indeed, the high-resolution HAADF-STEM image of

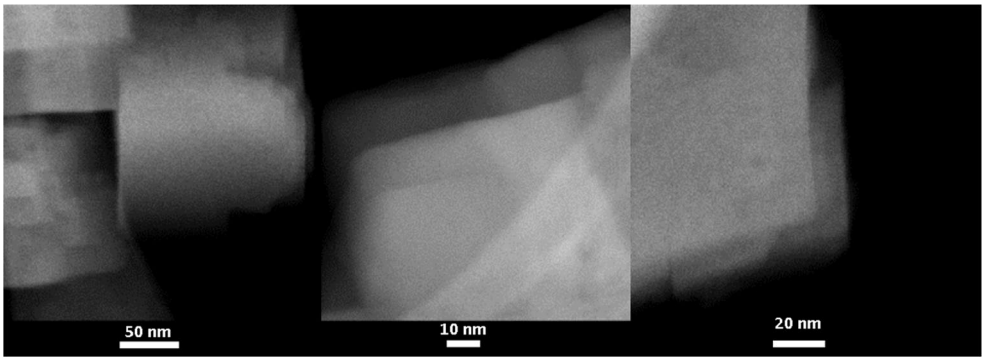

Fig. 13 Cryo-HAADF-STEM images of 1 wt% Pd/SSZ13 with Si/Al ratio 6 showing very high dispersion of Pd (no agglomeration)

the hydrothermally aged sample still shows the abundance of atomically dispersed species in the channels (Fig. 15). Particles on the external surface are relatively sparse, confirming that only a fraction of Pd is removed from the pores, forming relatively large PdO agglomerates, in agreement with XRD.

Additionally, HAADF-STEM images also reveal the formation of micro- and mesopores (defects) in the SSZ-13 crystals (circled in red, darker areas) due to the steaming procedure [26].

Since even for 3 wt% Pd/SSZ-13 with Si/Al = 6 we were able to achieve ~ 90% atomic dispersion of Pd, we exposed this material to 2 cycles of HTA. The NOx uptake profiles after each high-temperature hydrothermal aging cycle are presented in Fig. 16.

The result is consistent with the performance decrease of 1 wt% Pd/SSZ-13 samples: HTA under these harsh conditions leads to ~ 15% loss of NOx storage capacity for the 3 wt% Pd/SSZ-13 sample. Subjecting the same sample to the second cycle of aging leads to an additional approximately 15% loss of NOx storage capacity. The robustness of Pd/SSZ-13 samples with initially atomically and mostly atomically dispersed Pd as NOx adsorbers is quite notable.

Another question that arises at this point: can the activity of Pd/SSZ-13 samples after deactivation by various treatments be restored? For example, ($NO+O_2$) mixture is known to cause oxidation (and thus redispersion) of metallic particles, while reduction followed by oxidative treatment could also lead some changes in activity. We performed such treatments on HTA 1 wt% Pd/SSZ-13 (Si/Al ~ 12) and the results obtained are displayed in Fig. 17. We applied two distinctly different post-HTA treatment: (1) oxidation in $NO+O_2$ at 400 °C for 1 h, and (2) reduction in CO at 400 °C for 1 h followed by oxidation in an O_2 flow at 650 °C. Neither of these treatments were able to restore the activity of the aged sample to its initial level; however, the PNA performance remained practically unchanged.

Why did not Pd re-disperse? It is straightforward to explain based on the fact that the loss of atomically dispersed Pd is caused not by simple agglomeration but by agglomeration induced by the loss of framework Al sites. Since this process leaves defects in the framework and Al does not go back into

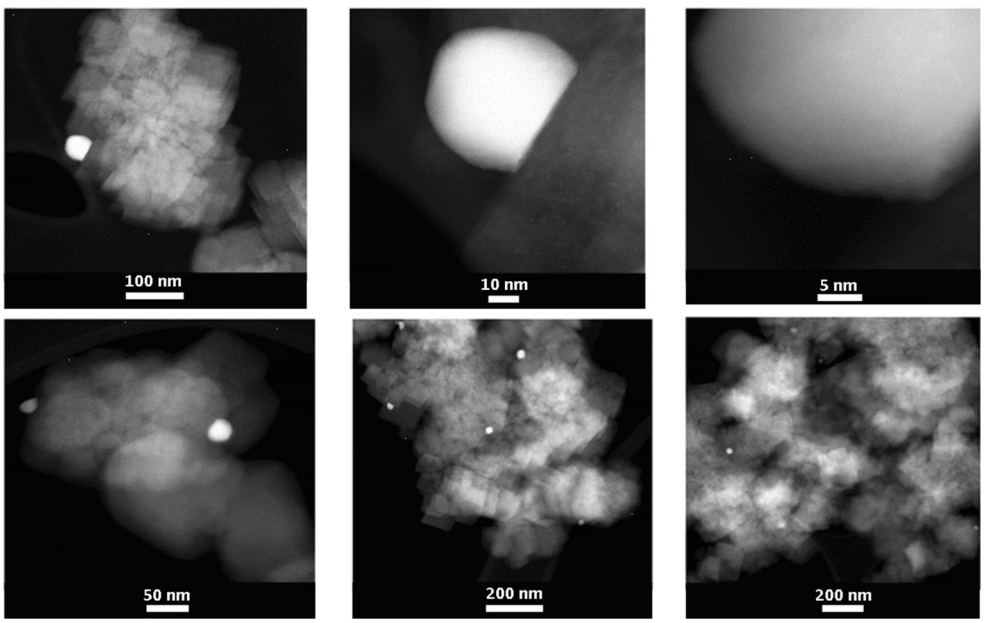

Fig. 14 HAADF-STEM images of different crystals/parts 1 wt% Pd/SSZ13 with Si/Al ratio 6 after hydrothermal aging at 750 °C for 16 h in 10% H_2O/air flow

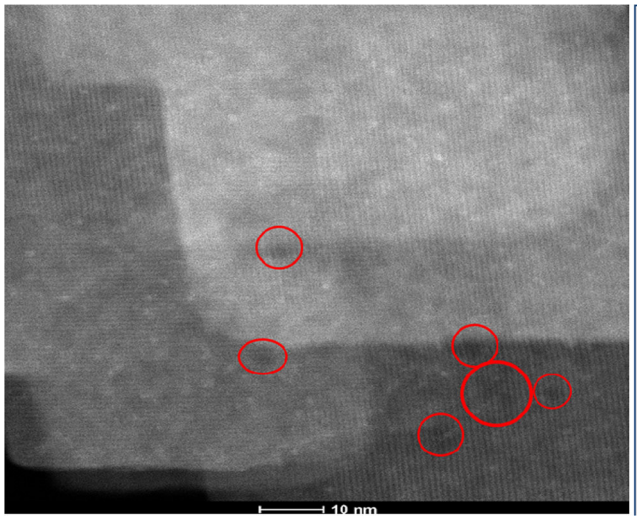

Fig. 15 High-resolution HAADF-STEM image of 1 wt% Pd/SSZ13 with Si/Al ratio 6 after hydrothermal aging at 750 °C for 16 h in 10% H_2O/air flow. The bright spots are Pd entities in the pores

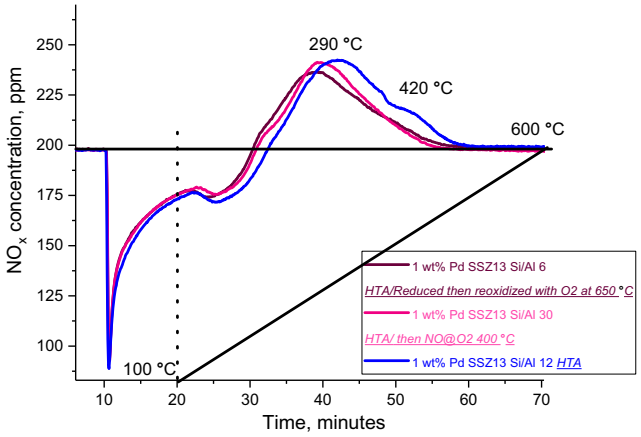

Fig. 17 NOx adsorption at 100 °C for 10 min followed with TPD (10 °C/min linear ramp rate) for 1 wt% Pd/SSZ-13 Si/Al ~ 12 HTA. Conditions, 120 mg of the sample, 210 sccm/min flow rate. The feed gas mixture contains ~ 200 ppm of NOx (190 ppm of NO and 10 ppm of NO_2) balanced with N_2 at a flow rate of 210 sccm with 14% O_2, 200 ppm CO, and 2.7% H_2O

those defects to heal them, the Pd does not easily re-disperse (the number of anchoring sites is reduced by the dealumination). Alternatively, it may be the size of PdO nanoparticles being too large preventing their redispersion. Indeed, it is known that larger nanoparticles are known to be harder to re-disperse than small clusters due to their higher inherent stability.

From the abovementioned experiments, it also becomes clear that pre-reduction should lead to the decrease in PNA activity. To test this, we pre-reduced the 1 wt% Pd/SSZ-13 sample (Si/Al = 30) with CO at 400 °C, and we indeed observed significant drop of NOx storage capacity (Fig. 18).

3.6 Direct Infrared Spectroscopic Evidence of Changes in both Pd(II) and Bronsted Acid Site Distribution in Pd/SSZ-13 after Hydrothermal Aging Using NO as a Probe Molecule

In order to identify the NOx species adsorbed on the PNA materials during the uptake process, we conducted FTIR measurements on the fresh and HTA Pd/SSZ-13 samples (Si/Al = 12). FTIR is the most sensitive technique that can provide complete speciation of M-NO species. The infrared signature of chemisorbed NO, due to its high molar absorption coefficient [28–32], is a commonly used probe to identify the state and distribution of metal and other species present in supported

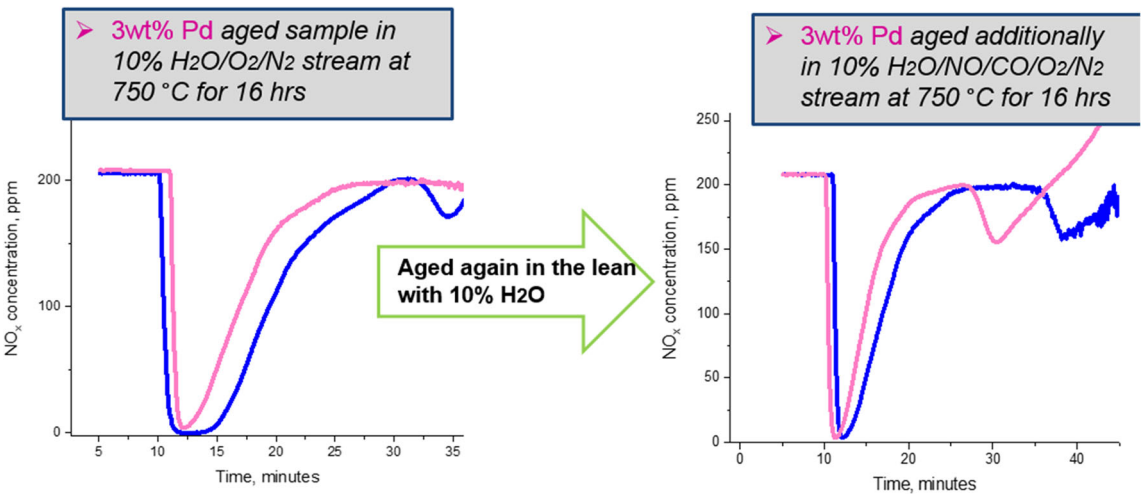

Fig. 16 NOx adsorption at 100 °C for 10 min followed with TPD (10 °C/min) for 3 wt% Pd/SSZ-13 with Si/AL ~ 6. Conditions, 120 mg of the sample, 310 sccm/min flow rate. The feed gas mixture contains ~ 200 ppm of NOx (190 ppm of NO and 10 ppm of NO_2) balanced with N_2 at a flow rate of 310 sccm with 14% O_2, 200 ppm CO, and 2.7% H_2O. Blue plot refers to the first sample, pink plot refers to the consequently tested aged sample: for the graph on the right side, the sample aged once (the same as the pink one on the left graph) on that graph is aged once again (thus, on that right graph, the once aged sample is denoted as blue, the one aged again after the first aging treatment is denoted as pink)

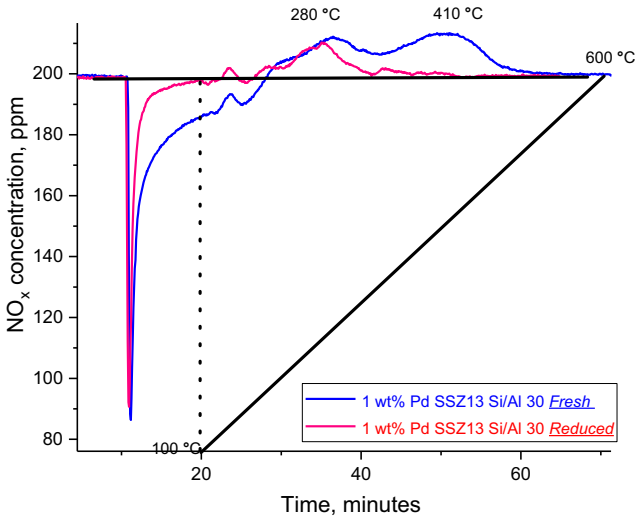

Fig. 18 NOx adsorption at 100 °C for 10 min followed with TPD (10 °C/min linear ramp rate) for 1 wt% Pd/SSZ-13 Si/Al ~ 30. Conditions, 120 mg of the sample, 210 sccm/min flow rate. The feed gas mixture contains ~ 200 ppm of NOx (190 ppm of NO and 10 ppm of NO_2) balanced with N_2 at a flow rate of 210 sccm with 14% O_2, 200 ppm CO, and 2.7% H_2O

transition metal complexes/cluster/nanoparticles. We have already shown that NO^+ can form upon NO and ($NO+O_2$) exposure of H/ and Pd/SSZ-13 samples, replacing Bronsted acid sites [15, 18, 19]. The position and intensity of the IR bands representing such species provide useful information regarding Brönsted acid sites in zeolites. Although, we cannot probe Brönsted acid sites directly, NO^+ occupying their positions can provide direct information about the occupied sites (vide infra). Stepwise NO adsorption (to a maximum P_{NO} of 0.2 Torr) on 1 wt% Pd/SSZ-13 (Si/Al = 12), monitored with FTIR, before and after HTA is shown in Fig. 19.

The IR results are in agreement with the observed decrease in NOx storage after HTA. Indeed, we observe visible decreases in the intensities of Pd-bound NO complexes. The N-O stretching bands belonging to Pd(I/II)-NO [18, 19] complexes are less intense in the aged sample, indicating the loss of available atomically dispersed Pd. In the hydrothermally aged sample, beside the decrease in the number of framework Al ions, the Al site distribution is also changed. This, in turn, leads to different isolated Pd ion distribution that manifests itself in the changing intensity ratio of the Pd-bound NO species. Furthermore, the nitrosonium ions occupying Brönsted acid sites, characterized by a relatively broad band at ~ 2190 cm^{-1} in the fresh sample, are significantly diminished and shifted to lower wavenumbers in the hydrothermally aged sample. It is evident that the Brönsted acidity in the aged sample significantly erodes and the nature of Brönsted acid sites changes upon dealumination with the formation of weaker Brönsted acid sites. For the first time, we show that the strength of Brönsted acid sites can be directly assessed by the shift of the N-O stretching frequency to lower wavenumbers, i.e., the electron withdrawing ability of framework atoms decreases, thus producing less acidic H-O sites. This novel result is consistent and complementary to the ^{27}Al NMR data.

3.7 Conclusions

Pd ions supported on various zeolites (SSZ-13, BEA, ZSM-5) are suitable for use as low-temperature passive NOx adsorbers. Active species in those materials are atomically dispersed Pd, and thus, their NOx storage capacity is directly proportional to the amount of isolated Pd ions in zeolite micropores. Different pore architectures of such materials lead to different NOx release temperatures. Abundant Brönsted acid sites and absence of other ions, such as sodium (potassium and others), are key to maintaining atomic dispersion of Pd and relevant PNA performance.

Using sensitive synchrotron XRD data, we compared fresh and aged Pd/zeolite samples and detected the formation of

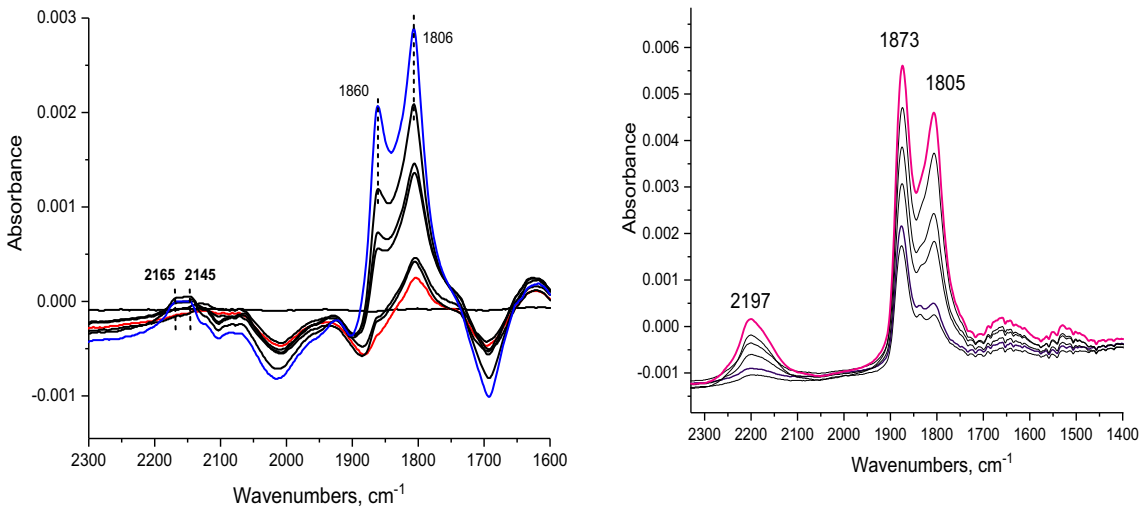

Fig. 19 FTIR during 0.2 Torr NO adsorption on the fresh 1 wt% Pd/SSZ-13 Si/Al ~ 12 sample (right graph) and aged (left graph)

PdO nanoparticles after hydrothermal aging at 750 °C for 16 h in 10% water vapor/air flow.

High-field MAS ^{27}Al solid-state NMR provided invaluable insight into changes to the zeolite after hydrothermal aging. Hydrothermal aging leads to loss of framework tetrahedral Al sites as well as broadening of their coordination environments within zeolite, with the concomitant formation of penta-coordinated and some octa-coordinated Al species.

HAADF-STEM imaging allowed us to visualize the fate of initially atomically dispersed Pd sites: due to the loss of framework Al sites that serve as anchors for Pd ions, Pd agglomerates into large (> 10 nm) PdO nanoparticles on the external surface of zeolite crystals during hydrothermal aging (HTA). However, the majority of atomically dispersed Pd in 1–3 wt% Pd/SSZ-13 Si/Al ~ 6 samples remains atomically dispersed in the micropores of zeolite, leading to the PNA storage loss of ~ 10–15% after prolonged aging (750 °C for 16 h in the presence of 10% water vapor in the flow of air). In order to restore the PNA performance, the PdO nanoparticles need to be re-dispersed back to the single atoms in ion exchange positions of zeolites. However, the agglomerated, bulk-like PdO nanoparticles cannot be easily re-dispersed due to the significant depletion in the amount and decrease in acidity of the Brönsted acid sites, confirmed by FTIR studies with NO as a probe molecule. The inherent stability of such large PdO nanoparticles prevents their redispersion in the absence of strong and abundant Brönsted acid protons. Thus, resistance of Pd/zeolite PNA materials to hydrothermal aging is intimately related to the stability of framework toward dealumination: more stable frameworks, like SSZ-13, are better candidates to support Pd ions in their micropores then ZSM-5 and Beta [33–38].

Despite the aforementioned PdO agglomeration process that takes place during HTA, we highlight the great potential of fresh Pd/SSZ-13 with atomically dispersed Pd to resist the damage and consequential loss of performance during HTA. We show that it is indeed possible to produce remarkably active and hydrothermally resistant Pd/SSZ-13 passive NOx adsorbers, starting with highly loaded atomically dispered Pd/zeolite materials.

Acknowledgements We gratefully acknowledge the U.S. Department of Energy (DOE), Office of Energy Efficiency and Renewable Energy, Vehicle Technologies Program for the support of this work. Most of the research described in this paper was performed in the Environmental Molecular Sciences Laboratory (EMSL), a national scientific user facility sponsored by the DOE's Office of Biological and Environmental Research and located at the Pacific Northwest National Laboratory (PNNL). PNNL is operated for the US DOE by Battelle.

Compliance with Ethical Standards

Competing Interest KK, JSz, LK, NJ, FG, and YW filed for a patent.

References

1. Khair, M.K., Majewski, W.A.: Diesel emissions and their control. SAE International, Warrendale (2006)
2. Forzatti, P., Nova, I., Tronconi, E.: New "enhanced NH3-SCR" reaction for NOx emission control. Ind. Eng. Chem. Res. **49**(21), 10386–10391 (2010)
3. Beale, A., Gao, F., Lezcano-Gonzalez, I., Peden, C., Szanyi, J.: Recent advances in automotive catalysis for NOx emission control by small-pore microporous materials. Chem. Soc. Rev. **44**(20), 7371–7405 (2015)
4. Melville, J. E., Brisley, R. J., Keane, O., Phillips, P. R., Mountstevens, E. H.: US Patent US8105559B2 (2012)
5. Cole, J. A.: US Patent US5656244A (1997)
6. Murata, Y., Morita, T., Wada, K., Ohno, H.: NOx trap three-way catalyst (N-TWC) concept: TWC with NOx adsorption properties at low temperatures for cold-start emission control. SAE Int. J. Fuels Lubr. **8**(2), 454–459 (2015)
7. Rajaram, R. R., Chen, H.-Y., Liu, D.: US Patent US20150158019A1 (2015)
8. Chen, H.-Y., Collier, J.E., Liu, D., Mantarosie, L., Duran-Martin, D., Novak, V., Rajaram, R., Thompsett, D.: Low temperature NO storage of zeolite supported Pd for low temperature diesel engine emission control. Catal. Lett. **146**, 1706–1711 (2016)
9. Ji, Y., Bai, S., Crocker, M.: Al_2O_3-based passive NOx adsorbers for low temperature applications. Appl. Catal. B Environ. **170–171**, 283–292 (2015)
10. Jones, S., Ji, Y., Crocker, M.: CeO_2-M_2O_3 passive NOx adsorbers for cold start applications, CLEERS Workshop (2016)
11. Zheng, Y., Kovarik, L., Engelhard, M.H., Wang, Y., Wang, Y., Gao, F., Szanyi, J.: Low-temperature Pd/zeolite passive NOx adsorbers: structure, performance, and adsorption chemistry. J. Phys. Chem. C. **121**(29), 15793–15803 (2017)
12. Theis, J.R., Lambert, C.K.: Mechanistic assessment of low temperature NOx adsorbers for cold start NOx control on diesel engines. Catal. Today. (2017) In Press
13. Vu, A., Luo, J., Li, J., Epling, W.S.: Effects of CO on Pd/BEA passive NOx adsorbers. Catal. Lett. **147**, 745–750 (2017)
14. Ryou, Y., Lee, J., Lee, H., Kim, C.H., Kim, D.H.: Effect of various activation conditions on the low temperature NO adsorption performance of Pd/SSZ-13 passive NOx adsorber. Catal. Today. (2017) In Press
15. Khivantsev, K., Gao, F., Kovarik, L., Wang, Y., Szanyi, J.: Molecular level understanding of how oxygen and carbon monoxide improve NOx storage in palladium/SSZ-13 passive NOx adsorbers: the role of NO^+ and Pd(II)(CO)(NO) species. J. Phys. Chem. C. **122**(20), 10820–10827 (2018)
16. Camblor, M.A., Corma, A., Valencia, S.: Synthesis in fluoride media and characterisation of aluminosilicate zeolite beta. J. Mater. Chem. **8**(9), 2137–2145 (1998)
17. Prodinger, S., Shi, H., Wang, H., Derewinski, M.A., Lercher, J.A.: Impact of structural defects and hydronium ion concentration on the stability of zeolite BEA in aqueous phase. Appl. Catal. B Environ. **237**, 996–1002 (2018)
18. Khivantsev, K., Jaegers, N.R., Kovarik, L., Hanson, J.C., Tao, F.F., Tang, Y., Zhang, X., Koleva, I.Z., Aleksandrov, H.A., Vayssilov, G.N., Wang, Y., Gao, F., Szanyi, J.: Achieving atomic dispersion of highly loaded transition metals in small-pore zeolite SSZ-13: high-capacity and high-efficiency low temperature CO and passive NOx adsorbers. Angew. Chem. Int. Ed. **57**(51), 16672–16677 (2018)
19. Khivantsev, K., Jaegers, N.R., Kovarik, L., Prodinger, S., Derewinski, M.A., Wang, Y., Gao, F., Szanyi, J.: Palladium/beta zeolite passive NOx adsorbers (PNA): clarification of PNA chemistry and the effects of CO and zeolite crystallite size on PNA performance. App. Cat. A. **569**, 141–148 (2019)

20. Khivantsev, K., Jaegers, N.R., Koleva, I.Z., Aleksandrov, H.A., Kovarik, L., Engelhard, M., Gao, F., Wang, Y., Vayssilov, G., Szanyi, J.: Stabilization of super electrophilic Pd+2 cations in small-pore SSZ-13 zeolite, Chemrxiv (2019) https://doi.org/10.26434/chemrxiv.7789454
21. Lee, J., Ryou, Y., Hwang, S., Kim, Y., Cho, S.-J., Lee, H., Kim, C., Kim, D.H.: Catal. Sci. Technol. **9**, 163–173 (2019)
22. Kovarik, L., Washton, N.M., Kukkadapu, R., Devaraj, A., Wang, A., Wang, Y., Szanyi, J., Peden, C.H.F., Gao, F.: Transformation of active sites in Fe/SSZ-13 SCR catalysts during hydrothermal aging: a spectroscopic, microscopic, and kinetics study. ACS Catal. **7**, 2458–2470 (2017)
23. Gao, F., Walter, E.D., Kollar, M., Wang, Y., Szanyi, J., Peden, C.H.F.: Understanding ammonia selective catalytic reduction kinetics over Cu/SSZ-13 from motion of the Cu ions. J. Catal. **319**, 1–14 (2014)
24. Jaegers, N.R., Wan, C., Hu, M.Y., Vasiliu, M., Dixon, D.A., Walter, E., Wachs, I.E., Wang, Y., Hu, J.Z.: Investigation of silica-supported vanadium oxide catalysts by high-field 51V magic-angle spinning NMR. J. Phys. Chem. C. **121**(11), 6246–6254 (2017)
25. Hu, J.Z., Zhang, X., Jaegers, N.R., Wan, C., Graham, T.R., Hu, M., Pearce, C.I., Felmy, A.R., Clark, S.B., Rosso, K.M.: Transitions in Al coordination during gibbsite crystallization using high-field 27Al and 23Na MAS NMR spectroscopy. J. Phys. Chem. C. **121**(49), 27555–27562 (2017)
26. Qin, Z., Cychosz, K.A., Melinte, G., El Siblani, H., Gilson, J.-P., Thommes, M., Fernandez, C., Mintova, S., Ersen, O., Valtchev, V.: Opening the cages of faujasite-type zeolite. J. Am. Chem. Soc. **139**(48), 17273–17276 (2017)
27. Kwak, J.H., Lee, J.H., Burton, S.D., Lipton, A.S., Peden, C.H.F., Szanyi, J.: A common intermediate for N_2 formation in enzymes and zeolites: side-on Cu–nitrosyl complexes. Angew. Chem. Int. Ed. **52**(38), 9985–9989 (2013)
28. Hadjiivanov, K.I.: Identification of neutral and charged NxOy surface species by IR spectroscopy. Catal. Rev. Sci. Eng. **42**, 71–144 (2000)
29. Hadjiivanov, K., Saussey, J., Freysz, J.L., Lavalley, J.C.: FT-IR study of NO + O_2 co-adsorption on H-ZSM-5: re-assignment of the 2133 cm^{-1} band to NO^+ species. Catal. Lett. **52**(1/2), 103–108 (1998)
30. Szanyi, J., Paffett, M.T.: The adsorption of NO and reaction of NO with O_2 on H-, NaH-, CuH-, and Cu-ZSM-5: an in situ FTIR investigation. J. Catal. **164**(1), 232–245 (1996)
31. Khivantsev, K., Vityuk, A., Aleksandrov, H.A., Vayssilov, G.N., Blom, D., Alexeev, O.S., Amirdis, M.D., et al.: ACS Catal. **7**, 5965–5982 (2017)
32. Khivantsev, K., Vityuk, A., Aleksandrov, H.A., Vayssilov, G.N., Alexeev, O.S., Amirdis, M.D.: Effect of Si/Al ratio and Rh precursor used on the synthesis of HY zeolite-supported rhodium carbonyl hydride complexes. J. Phys. Chem. C. **119**(30), 17166–17181 (2015)
33. Epling, W.S., Campbell, L.E., Yezerets, A., Currier, N.W., Parks, J.E.: Overview of the fundamental reactions and degradation mechanisms of NOx storage/reduction catalysts. Catal. Rev. Sci. Eng. **46**, 163–245 (2004)
34. Choi, J.S., Partridge, W.P., Lance, M.J., Walker, L.R., Pihl, J.A., Toops, T.J., Finney, C.E.A., Daw, C.S.: Nature and spatial distribution of sulfur species in a sulfated barium-based commercial lean NOx trap catalyst. Catal. Today. **151**, 354–361 (2010)
35. Lietti, L., Forzatti, P., Nova, I., Tronconi, E.J.: NOx storage reduction over Pt Ba/γ-Al_2O_3 catalyst. J. Catal. **204**, 175–191 (2001)
36. Kim, D.H., Mudiyanselage, K., Szanyi, J., Zhu, H., Kwak, J.H., Peden, C.H.F.: Characteristics of Pt-K/MgAl2O4 lean NOx trap catalysts. Catal. Today. **184**, 2–7 (2012)
37. Alikhani, M.E., Krim, L., Manceron, L.: Infrared spectra and structures of nickel and palladium dinitrosyl complexes isolated in solid argon. J. Phys. Chem. A. **105**, 7817–7822 (2001)
38. Mintova, S., Gilson, J.P., Valtchev, V.: Advances in nanosized zeolites. Nanoscale. **5**(15), 6693–6703 (2013)